

Winter Upper-Ocean Stability and Ice–Ocean Feedbacks in the Sea Ice–Covered Southern Ocean

EARLE A. WILSON, STEPHEN C. RISER, ETHAN C. CAMPBELL, AND ANNIE P. S. WONG

School of Oceanography, University of Washington, Seattle, Washington

(Manuscript received 13 September 2018, in final form 17 January 2019)

ABSTRACT


In this study, under-ice ocean data from profiling floats, instrumented seals, and shipboard casts are used to assess wintertime upper-ocean stability and heat availability in the sea ice–covered Southern Ocean. This analysis reveals that the southern Weddell Sea, which features a weak upper-ocean stratification and relatively strong thermocline, is preconditioned for exceptionally high rates of winter ventilation. This preconditioning also facilitates a strong negative feedback to winter ice growth. Idealized experiments with a 1D ice–ocean model show that the entrainment of heat into the mixed layer of this region can maintain a near-constant ice thickness over much of winter. However, this quasi-equilibrium is attained when the pycnocline is thin and supports a large temperature gradient. We find that the surface stress imparted by a powerful storm may upset this balance and lead to substantial ice melt. This response can be greatly amplified when coincident with anomalous thermocline shoaling. In more strongly stratified regions, such as near the sea ice edge of the major gyres, winter ice growth is weakly limited by the entrainment of heat into the mixed layer. Thus, the thermodynamic coupling between winter sea ice growth and ocean ventilation has significant regional variability. This regionality will influence the response of the Southern Ocean ice–ocean system to future changes in ocean stratification and surface forcing.

1. Introduction

In the sea ice–covered Southern Ocean, a relatively thin halocline separates the cold winter mixed layer (ML) from the significantly warmer ocean interior (Gordon and Huber 1984). Over the course of winter, this halocline is gradually eroded by convective instabilities, triggered by the brine released from sea ice growth (Gordon et al. 1984). In some regions, such as the weakly stratified Weddell Sea, the halocline is typically eroded to the point where a relatively small addition of brine would completely eliminate the main pycnocline and permit uninhibited convection into the ocean interior (Martinson and Iannuzzi 1998, hereafter M98). However, such deep convective events are rarely observed, and the ML in these regions is generally confined to the upper 200 m (Gordon and Huber 1990; Pellichero et al. 2017). The somewhat surprising resilience of this weak winter stratification is largely due to the upper

ocean's negative feedback to ice growth (Martinson 1990, hereafter M90). As the ML deepens, the entrained heat provides a basal heat flux to the sea ice that suppresses further ice growth and, in some cases, causes melt that restratifies the upper ocean (McPhee et al. 1999). Thus, the winter temperature profile, despite featuring a cold-over-warm water configuration, helps to maintain the stability of the water column by limiting the destabilizing effect of sea ice growth. On the rare occasions that sustained deep convection does occur, the ventilated heat creates vast areas of open water within the sea ice zone. The most dramatic examples of such an event are the Weddell Sea polynyas that occurred during the winters of 1974–76. At their peak, these polynyas occupied a large portion of the Weddell Sea and featured convection down to at least 4000 m (Gordon 1978). Since then, no winter polynya of a similar magnitude or duration has occurred in the Southern Ocean.

The main source of deep ocean heat in this region is Circumpolar Deep Water (CDW) (Foster and Carmack 1976). This water mass is progressively cooled as it is upwelled and circulated within the polar gyres of the region (Fahrbach et al. 1994). The resulting modified

 Denotes content that is immediately available upon publication as open access.

Corresponding author: Earle A. Wilson, earlew@uw.edu

CDW is a major source of heat for the shelf waters of Antarctica and, by extension, the marine terminating glaciers of the Antarctic Ice Sheet (Jacobs et al. 1985; Pritchard et al. 2012). This water mass is also a key end-member in the formation of Antarctic Bottom Water (AABW), which is exported to most of the global abyssal ocean (Gill 1973; Johnson 2008). Thus, the wintertime ventilation of the deep ocean in the sea ice zone directly modulates the flow of heat to the Antarctic continental margin and helps set the properties of Antarctic Bottom Water (AABW).

Though the ventilation of heat in the Antarctic sea ice zone has been the focus of many studies, our understanding of its spatial and temporal variability has been limited by the historical lack of in situ winter ocean data. Prior to the early 2000s, winter ocean data were mainly collected during sporadic research cruises conducted on icebreakers. Since then, two recent advances in observational oceanography have led to a dramatic increase in wintertime under-ice ocean data. The first is the introduction of Argo floats equipped with ice-avoidance algorithms that allow them to safely profile in the presence of sea ice (Klatt et al. 2007; Wong and Riser 2011). The second is the advent of animal-borne sensor programs that have equipped hundreds of seals with satellite-linked conductivity–temperature–depth (CTD) sensors (Roquet et al. 2013). Together, under-ice Argo floats and instrumented seals have provided unprecedented year-round coverage of the oceans around Antarctica.

The primary goal of this study is to better understand the relationship between wintertime upper-ocean stability, deep ocean ventilation, and sea ice growth in the Southern Ocean. Our analysis borrows heavily from the conceptual framework laid out by M90 and M98. In particular, we use modified versions of their bulk stability metrics to diagnose upper-ocean stability and the availability of deep ocean heat in the winter sea ice zone. By using more recent winter CTD data, we are able to expand on these previous studies, which have focused on the Weddell region. Additionally, we combine these observations with a simple 1D ice–ocean model to diagnose the coupling between winter ice growth and the entrainment of heat into the ML. This work is complementary to the recent ML analysis presented by Pellichero et al. (2017), who use a similar set of CTD observations. While they focus on the seasonal evolution of ML properties in the Southern Ocean, we focus exclusively on the winter season and investigate the thermodynamic coupling between ice growth and ocean ventilation in more detail.

In the next section, we describe our data and analysis techniques. This is followed by a presentation of our

observational analysis and idealized model simulations. We conclude with a summary of our key findings.

2. Data acquisition and processing

a. CTD profiles

The primary observations used in this study are CTD profiles collected by Argo floats, instrumented seals, and ship-based casts. Argo float data were acquired from the March 2018 snapshot of the Argo Global Data Assembly Centre (GDAC) database (Argo 2018). We used the “adjusted” CTD profiles, which have been modified to eliminate known biases, and retained profiles for which each measurement was flagged as data of “good” quality (QC flag = 1). The seal-based data were obtained from the November 2017 release of the Marine Mammal Exploring the Oceans Pole-to-Pole (MEOP) CTD database (Roquet et al. 2017). These data were provided in the format as the GDAC database. As before, we retained adjusted profiles that passed all quality control checks (QC flag = 1). The ship-based data were acquired from the NOAA World Ocean Database (<https://www.nodc.noaa.gov/OC5/SELECT/dbsearch/dbsearch.html>), which was accessed on 1 February 2018. We selected profiles collected by high-resolution CTD casts and ocean station bottle data, saving only the profiles flagged as good (QC flag = 0).

Winter profiles from ships and instrumented seals are transmitted with relatively precise geographical coordinates. However, since Argo floats generally do not surface in the presence of sea ice, their exact coordinates are unknown during the winter (Wong and Riser 2011). The under-ice locations of these profiles are estimated via linear interpolation. This captures the mean trajectory of the float over the course of winter, but neglects any deviations caused by eddies or topographical effects. We assume that these positional errors are smaller than the basinwide scales that are of interest in this study.

To ensure that each profile accurately resolves the key features of the upper ocean, specifically the ML and the pycnocline, we filtered for profiles that extend deeper than 300 m and have more than five data points above that depth level. Additionally, we only retained profiles that have data points above 25 m, which ensures that the properties of the ML are captured. Applying the first filter mainly affects the seal-based data, which have the coarsest vertical resolution. These profiles are transmitted via satellite in a compressed form that contains only 10–25 data points (Roquet et al. 2014). Since seals regularly dive beyond 500 m, the apparent vertical resolution of these profiles is on the order of tens of meters. However, the transmitted data points are chosen using

an algorithm that identifies the major inflection points of the CTD profile (Boehme et al. 2009). We therefore make the assumption that the seal-based profiles, though relatively coarse, still capture the key features of the upper ocean. The chosen profiles, from all sources, were then linearly interpolated to a common vertical coordinate that has a resolution of 0.5 m in the upper 500 m and progressively coarser spacing at deeper levels. Missing near-surface values were filled using nearest neighbor extrapolation.

For the winter season, which is defined here as June–September, Argo floats and instrumented seals are the largest contributors of CTD data (Fig. 1). Almost all of these data were collected within the past 15 years (Fig. 2). CTD profiles from Argo floats are broadly distributed across the sea ice zone, away from the Antarctic continental shelf. Profiles from seals are mostly found in the eastern Atlantic and Indian Ocean sectors, and along the western coast of the Antarctic Peninsula. The relatively few ship-based profiles are mainly from the Weddell region and near the Antarctic Peninsula. When composited in time, these three sources of data provide coverage for most of the winter sea ice zone.

Unless otherwise stated, all calculations (e.g., computing the mixed layer depth) are first applied to individual profiles and then spatially averaged over a given region. Spatial averages were computed for large regional domains of key interest and more localized 2° longitude \times 1° latitude grid boxes. No form of horizontal interpolation or smoothing was applied to these data.

b. Sea ice concentration

To define the winter sea ice zone, we used version 3 of the NOAA/NSIDC Climate Data Record (CDR) sea ice concentration product (Peng et al. 2013; Meier et al. 2017). With this data, which is provided on a $25\text{-km} \times 25\text{-km}$ spatial grid as monthly averages from August 1987 to February 2017, we constructed a climatology and defined the winter sea ice zone as the area within which the mean June–September sea ice concentration is greater than 15%.

3. Quantifying upper-ocean stability

In his seminal work, M90 introduced the salt deficit (SD) and thermal barrier (TB) diagnostics as measures of upper-ocean stability. SD represents the integrated freshwater anomaly of the ML and the halocline (see Fig. 3 for example winter profiles) and is defined as the sea ice growth that would cause the ML to entrain the entire halocline. TB is the integrated heat content of the halocline and thus quantifies the halocline’s capacity to provide a negative feedback to ice growth. M98 used

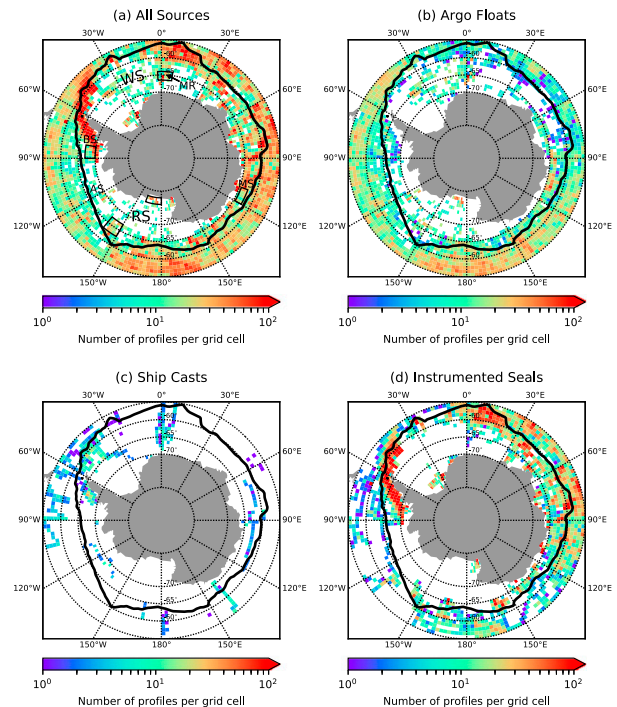


FIG. 1. The spatial distribution of winter CTD profiles binned on a 2° longitude \times 1° latitude grid. (a) Total number of profiles in each grid box. (b)–(d) Total number of profiles in each grid box from Argo floats, ship casts, and instrumented seals, respectively. Areas of interest are annotated in (a): Weddell Sea (WS), Ross Sea (RS), Maud Rise (MR), Bellingshausen Sea (BS), Amundsen Sea (AS), and Mawson Sea (MS). The boxes outline five subregions that are referenced in Figs. 3, 4, 8, and 10. In the Ross Sea region, the northern and southern boxes outline the northern Ross Sea and eastern Ross Shelf subregions, respectively.

all winter ship-based CTD data that were available at the time to quantify these metrics in the Weddell region. This analysis showed that, in most cases, roughly 1 m of additional winter sea ice growth would be enough to eliminate the local halocline and permit thermally driven convection in the ocean interior.

Here, we introduce slightly modified versions of SD and TB that account for the destabilizing effect of the winter temperature profile. These metrics provide an upper bound on the sea ice growth needed to erode the pycnocline and permit convection into the ocean interior. To obtain these metrics, we exploit the fact that winter mixed layer temperature (MLT) in the sea ice zone generally stays near the freezing point of seawater T_f (Gordon and Huber 1990). Mixed layer salinity (MLS), on the other hand, tends to increase throughout winter. If we take the winter MLT to be exactly T_f , we can find a critical MLS, S_c , that would allow the density of the ML to be equal to the density at some depth below the pycnocline. That is, we can determine S_c such that

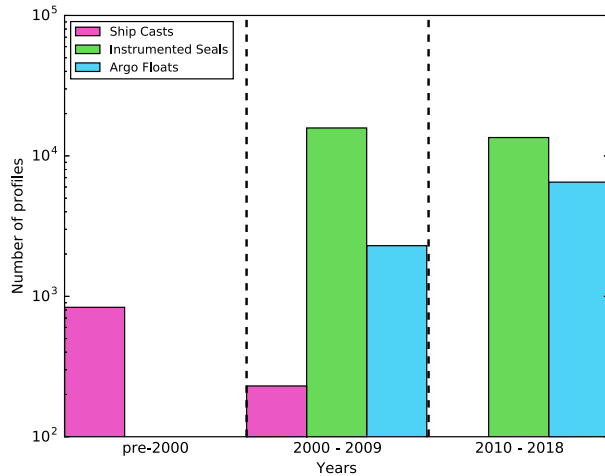


FIG. 2. Temporal distribution of June–September CTD profiles collected within the winter sea ice zone. Profiles are separated by source (Argo floats, ship casts, and instrumented seals) and time period (pre-2000, 2000–09, and 2010–18).

$$\sigma_{\text{ML}}(S_c, T_f, z = 0) = \sigma_d(S_d, T_d, z_d), \quad (1)$$

where σ is potential density referenced to the surface and subscript d indicates deep-ocean values, below the pycnocline. Parameter S_c can be determined numerically using a function for potential density, such as that provided in the Thermodynamic Equation of Seawater 2010 (TEOS-10) toolbox (McDougall and Barker 2011). In the northern Ross Sea and Maud Rise profiles, σ varies very little below 300 m (Fig. 3). This is true across the entire winter sea ice zone. This means the solution to (1) is insensitive to the choice of z_d provided it is below this depth. Since most profiles from instrumented seals have a maximum depth of 500 m, we use $z_d = 500$ m as our reference deep-ocean level.

The equality expressed in (1) is attained when the freshwater anomaly above the depth where $S(z) = S_c$ is removed from the upper ocean. Taking this critical depth to be z_c , we define the pycnocline salt deficit SD^* as

$$SD^* = \frac{1}{\Delta S_i} \int_0^{z_c} [S(z_c) - S(z)] dz. \quad (2)$$

where $S(z)$ is the upper-ocean salinity profile, and ΔS_i is the salinity difference between the ocean surface and sea ice. Following M98, we take ΔS_i to be 30 psu, assuming a typical sea ice salinity and MLS of 4 psu and 34 psu, respectively. SD^* has units of ice thickness (i.e., meters of required ice growth) and is analogous to the halocline SD metric introduced by M90. The pycnocline thermal barrier TB^* is defined as the total heat content between the base of the ML and the depth z_c . This is given by

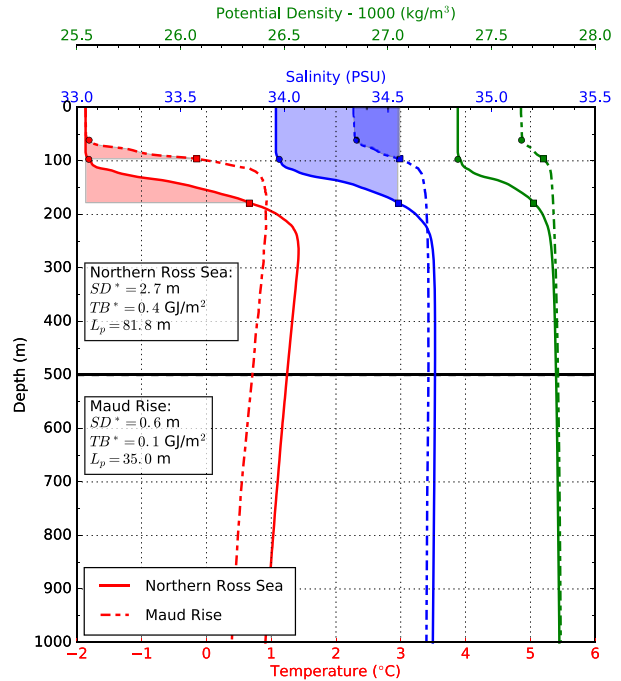


FIG. 3. Example early winter (June) profiles of temperature (red) and salinity (blue) from the Maud Rise (solid lines) and northern Ross Sea (broken lines) regions (see Fig. 1 for region boundaries). The blue and red shading show the area integrals used to compute the pycnocline salt deficit (SD^*) and thermal barrier (TB^*), respectively. Circle markers indicate the MLD, which is defined using a 0.02 kg m^{-3} density threshold. Square markers indicate z_c , the depth where salinity is equal to the critical MLS that would allow the potential density of the ML to be equal to that at 500 m [see (1) and the ensuing discussion]. Also labeled is L_p , which is pycnocline thickness; we define this term as the difference between MLD and z_c .

$$TB^* = \rho_w c_w \int_0^{z_c} [T(z) - \text{MLT}] dz, \quad (3)$$

where ρ_w is the density of seawater, c_w is the specific heat capacity of seawater, and $T(z)$ is the upper-ocean temperature profile. Unlike M98, we express TB^* in units of heat (J m^{-2}) rather than meters of potential ice melt. Last, since z_c approximately coincides with the base of the pycnocline (Fig. 3), we compute the thickness of the pycnocline L_p as

$$L_p = |z_c - \text{MLD}|, \quad (4)$$

where MLD refers to the mixed layer depth. Since the base of the pycnocline is not always well-defined and the transition into the ocean interior can be relatively smooth, we treat L_p as a rough vertical length scale for the pycnocline.

To arrive at (2) and (3), we neglect many non-ice-related processes that could alter upper-ocean stratification over the course of winter. Following M98, we

assume that changes in MLS due to precipitation are small compared to those due sea ice growth. This is a reasonable assumption for much of the winter sea ice zone, where the open-water fraction is generally less than 5% in the winter. The remaining processes that can modify upper-ocean salinity are horizontal stirring and vertical mixing across the base of the ML. On basinwide scales, the MLS tendency due to horizontal advection is small relative to the MLS changes associated with vertical mixing and ice–ocean freshwater fluxes (Pellichero et al. 2017). This may not be the case on smaller scales but, given the coarse spatial resolution of our CTD data, we do not attempt to quantify the effects of small-scale horizontal mixing. Vertical mixing across the base of the ML will tend to increase MLS. This vertical exchange may result from shear-induced mixing from wind and ice–ocean stresses, double diffusion, thermobaric instabilities, and internal wave breaking (Muench et al. 1990; McPhee and Martinson 1994; Robertson et al. 1995; Akitomo 1999). We do not attempt to quantify the impact of these vertical processes, which are poorly constrained across the winter sea ice zone. Nevertheless, observations suggest that sea ice growth is the primary driver of wintertime MLS variability underneath sea ice (Charrassin et al. 2008; Wong and Riser 2011). We therefore focus on salt fluxes from brine rejection and treat SD^* as an upper bound on the ice growth needed to permit thermally driven convection into the ocean interior. Furthermore, heat fluxes from the deep ocean may partially replenish the heat content of the pycnocline over the course of winter. TB^* is therefore a lower bound on the amount of heat that could be ventilated from the pycnocline.

As an example, we compute SD^* and TB^* for representative early winter profiles from the northern Ross Sea and Maud Rise regions (Fig. 3). These regions represent opposite extremes in off-shelf, upper-ocean stratification in the winter sea ice zone. Assuming a deep ocean reference level of 500 m, we find that $SD^* = 2.7$ m and $TB^* = 0.4 \text{ GJ m}^{-2}$ for the northern Ross Sea. This means 2.7 m of additional winter sea ice growth would weaken the haline stratification to the point where surface cooling, on its own, could drive convection down to 500 m. However, the production of 2.7 m of additional sea ice would ventilate (at minimum) 0.4 GJ m^{-2} of heat, which could melt approximately 1.3 m of sea ice. Over the more weakly stratified Maud Rise, these values are much lower, with $SD^* = 0.6$ m and $TB^* = 0.1 \text{ GJ m}^{-2}$.

Going a step further, if we divide TB^* by SD^* we obtain a measure for the *total* availability of heat in the pycnocline:

$$\gamma_p = \frac{TB^*}{SD^*}. \quad (5)$$

The quantity γ_p gives the average heat released per unit ice growth, in the event the entire pycnocline is entrained into the ML. However, in most regions, only a fraction of the pycnocline is eroded each winter. More importantly, the efficiency of heat ventilation (i.e., the heat released per unit ice growth) increases with the depth of entrainment. To demonstrate this, we introduce slightly more general definitions of the salt deficit and thermal barrier metrics that are functions of entrainment depth:

$$\eta(z') = \frac{1}{\Delta S_i} \int_0^{z'} [S(z') - S(z)] dz, \quad (6)$$

$$\nu(z') = \rho_w c_w \int_0^{z'} [T(z) - \text{MLT}] dz. \quad (7)$$

In the above equations, η is the sea ice growth needed to deepen the ML to some arbitrary depth z' while ν is the amount of heat that would be ventilated if the ML deepens to that level. When $z' = z_c$, η and ν are equivalent to SD^* and TB^* , respectively. Given the geometry of upper-ocean winter profiles of temperature and salinity, we find that $d\nu/dz' > d\eta/dz'$. This is because η represents the integrated salinity anomaly of the ML and some fraction of the pycnocline, while ν depends only on the heat stored in the pycnocline (Fig. 3). We note that below the pycnocline, $d\eta/dz'$ approaches zero while $d\nu/dz'$ tends toward some nonzero finite value. Furthermore, the quantity

$$\gamma(z') = \frac{\nu(z')}{\eta(z')}, \quad (8)$$

provides a depth-dependent metric that estimates the efficiency with which incremental sea ice growth can ventilate heat from the pycnocline.

4. Observational analysis

a. Upper-ocean properties in the winter sea ice zone

Between June and September, the ML in off-shelf regions of the sea ice zone has direct access to the main thermocline (Fig. 4). Here, MLD is defined using a density threshold of 0.02 kg m^{-3} . This relatively stringent density criterion is motivated by the need to accurately resolve the base of the winter ML in weakly stratified regions, such as near Maud Rise. After September, the ML begins to shoal as it transitions back to its summer state. This seasonality motivates

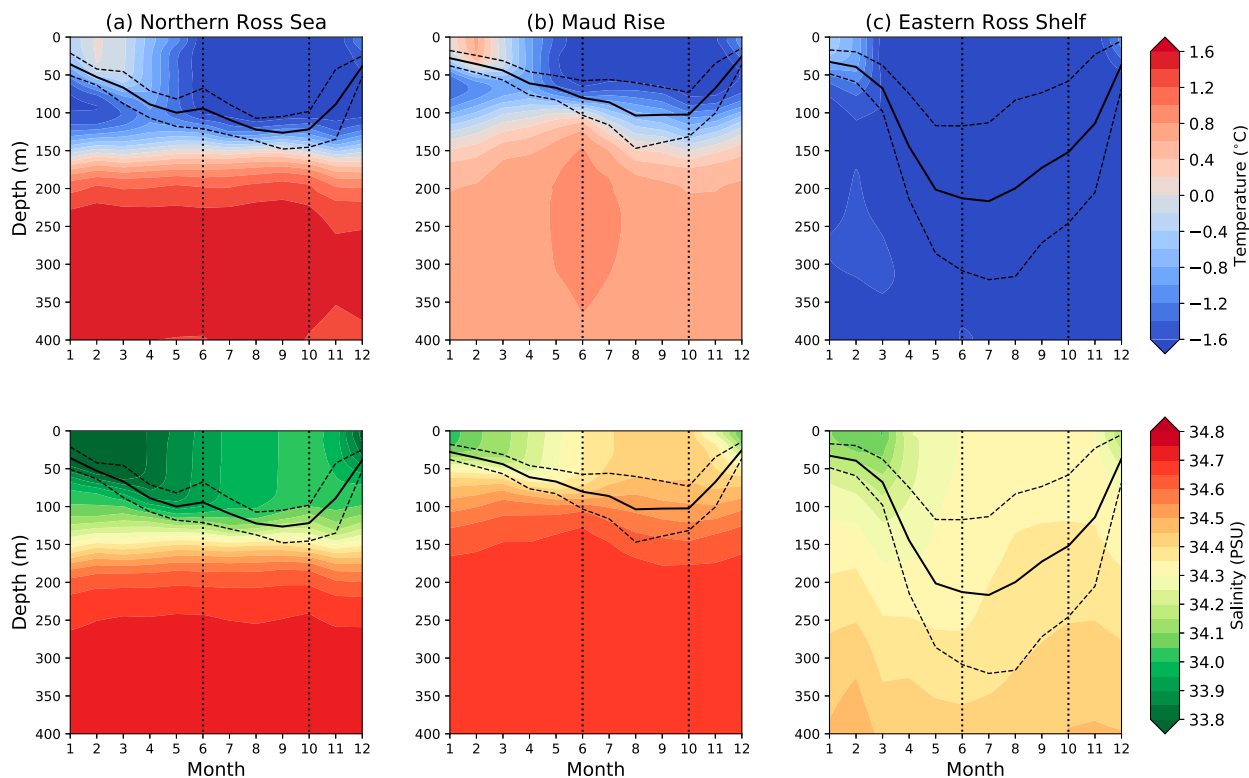


FIG. 4. Monthly mean upper-ocean (top) temperature and (bottom) salinity for the (a) northern Ross Sea, (b) Maud Rise, and (c) eastern Ross Shelf (see Fig. 1 for region boundaries). The solid black lines represent the monthly mean MLD, which is defined using a density threshold of 0.02 kg m^{-3} . The vertical distance between the solid and dashed lines represents one standard deviation of the monthly MLD for each region. The dotted vertical lines demarcate the winter season, which we define as June–September.

our choice to limit the winter season to June–September. Along the continental shelf, the water column typically lacks a well-defined thermocline and is usually uniformly near its freezing point during the winter (Fig. 4c). For this reason, we focus on off-shelf regions, where there is a distinct reservoir of deep ocean heat that can potentially modulate sea ice growth.

Winter MLS in the Atlantic sector, the region east of the Antarctic Peninsula that roughly extends from 60°W to 30°E , is $0.3\text{--}0.4$ psu higher than in the Pacific sector, west of the Peninsula (Fig. 5a). MLS in the Indian sector, along East Antarctica, is similar to that within the Atlantic sector, but has a stronger meridional gradient. This salinity gradient reflects the well-documented coastal production and northward export of sea ice around Antarctica (Drucker et al. 2011; Haumann et al. 2016). MLT is uniformly near the freezing point within the sea ice zone, but is several degrees warmer just beyond the ice edge. MLD varies between 75 and 125 m across off-shelf regions, but is significantly deeper along the continental shelf. These results are consistent with the ML analysis presented by Pellichero et al. (2017).

We quantify the strength of the halocline as the difference between the subsurface salinity maximum S_{max} and MLS. The spatial pattern of halocline strength mirrors that of MLS within the sea ice zone (Fig. 6a). In the Atlantic sector, the difference between S_{max} and MLS is generally less than 0.5 psu. In contrast, this salinity difference is generally greater than 0.6 psu in the Pacific sector. The spatial pattern of T_{max} is similar to that of halocline strength, but with notably weaker contrasts (Fig. 6b). In the Atlantic sector, near the Prime Meridian, the depth of T_{max} is generally shallower than 250 m (Fig. 6c). In extreme cases, T_{max} lies just tens of meters below the winter ML. These findings are consistent with previous studies that have mapped T_{max} across the Weddell region (e.g., Reeve et al. 2016). In other regions of the sea ice zone, T_{max} is generally deeper than 250 m. Finally, we compare the temperature difference ΔT across the thermocline (i.e., between the base of the ML and the depth of T_{max}) with the salinity difference ΔS across that layer. This highlights the southern Weddell as the region where the thermocline is strongest relative to the halocline (Fig. 6d). In this region, $\Delta T/\Delta S$ across the thermocline is generally between

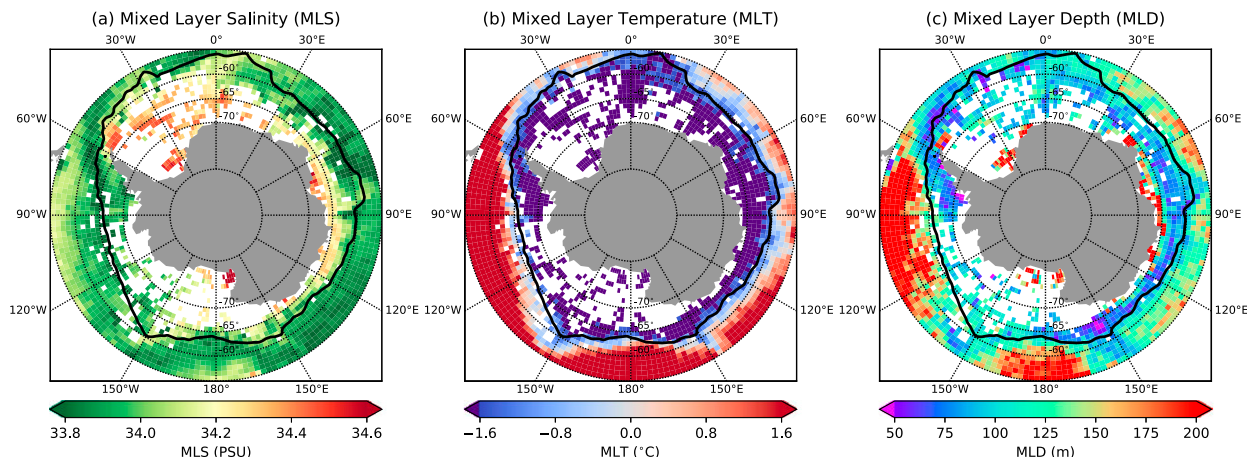


FIG. 5. Properties of the winter ML south of 55°S: (a) salinity, (b) temperature, and (c) depth. The solid black line represents the mean winter sea ice edge.

8° and 10°C psu^{-1} . Slightly lower values of $\Delta T/\Delta S$ are observed along the shelf break of East Antarctica and in the Ross Sea. $\Delta T/\Delta S$ is smallest in the eastern Pacific sector, where it mostly ranges between 4° and 6°C psu^{-1} .

In summary, upper-ocean stratification is exceptionally weak within the Atlantic sector and along the continental shelf. The off-shelf region within the Atlantic sector is particularly interesting because it features a weak halocline and a relatively shallow reservoir of deep ocean heat. This suggests that this region is preconditioned for the highest rates of wintertime heat ventilation.

b. Winter upper-ocean stability and heat availability

The regional pattern of SD^* (defined here using a reference deep ocean level of 500 m) is similar to that of MLS and halocline strength (Fig. 7a). In the Pacific sector, between 60°W and 180°, SD^* is generally greater than 2 m. This means the pycnocline in this region can support more than 2 m of additional winter ice growth before being completely eroded. In the Ross Sea and along East Antarctica, SD^* is slightly lower and varies between 1 and 2 m of additional winter sea ice growth. As expected, SD^* is relatively low across the interior of the Weddell, where it is generally less than 1.5 m. In particular, SD^* is less than 0.5 m in the vicinity of Maud Rise. However, SD^* exceeds 2 m along the winter ice edge of the Atlantic sector. The spatial pattern of SD^* in the Atlantic sector closely resembles that of SD , as presented by M98.

Except for areas with perennial sea ice, ice thickness in the late winter and early spring typically ranges between 0.4 and 0.8 m in the Southern Ocean (Worby et al. 2008; Kurtz and Markus 2012). As will be discussed later, this observed range of ice thickness is in part due

to the ventilation of heat from the thermocline. Outside the Weddell region, offshore values of SD^* far exceed the amount of in situ ice growth that normally occurs in a single year. Thus, we can conclude that full pycnocline erosion is highly unlikely to occur across most of the winter sea ice zone. However, in the Weddell region where SD^* is often less than the total winter ice growth, it is conceivable that variations in the annual surface freshwater budget could leave the region susceptible to full pycnocline erosion. This also suggests that the ventilation of sub-ML heat in this region, which limits ice growth, plays a crucial role in preventing the full erosion of the pycnocline.

Total pycnocline heat content, as quantified by TB^* , is relatively large in the eastern Pacific sector (Fig. 7b). In the Bellingshausen Sea, growing an amount of sea ice equivalent to the local value of SD^* would ventilate roughly 1 GJ m^{-2} (10^9 J m^{-2}), which would be sufficient to melt approximately 3 m of ice. TB^* is much smaller across the interior of the ice-covered Atlantic sector, where it is generally less than 0.3 GJ m^{-2} . In the Ross Sea and along East Antarctica, TB^* broadly varies between 0.1 and 0.7 GJ m^{-2} . In the former region, there is a distinct meridional contrast, with pycnocline heat content being relatively high just north of the continental shelf. The regional pattern of TB^* largely mirrors that of pycnocline thickness L_p , which varies from less than 25 m in the Atlantic sector to greater than 100 m in the eastern Pacific sector (Fig. 7c). This symmetry does not hold along the Antarctic coastal margin, where TB^* is very low despite L_p being relatively large.

The regional pattern of total pycnocline heat availability, quantified by $\gamma_p = TB^*/SD^*$, is similar to that of TB^* (Fig. 7d). By this metric, pycnocline heat is

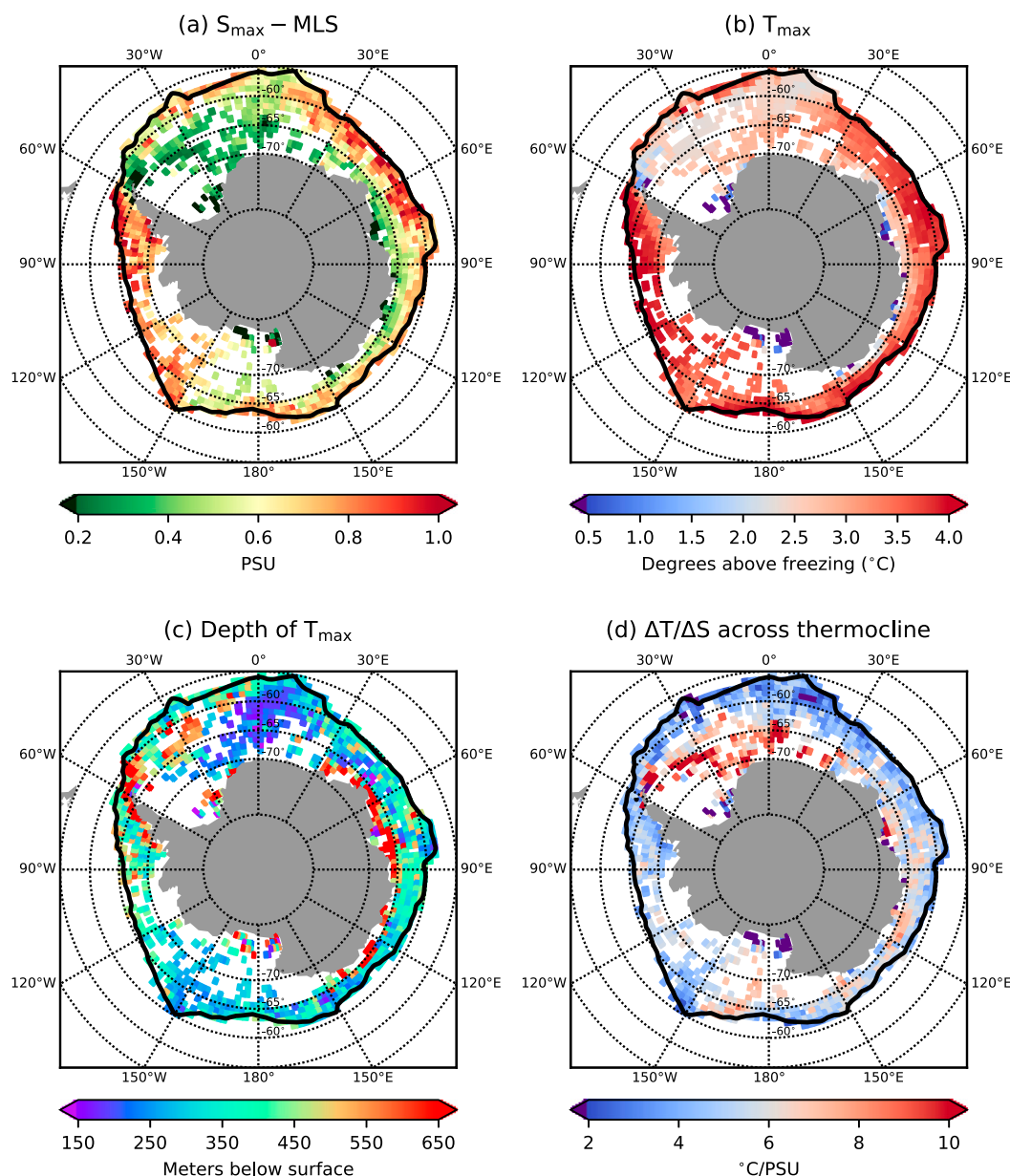


FIG. 6. Subsurface ocean properties within the winter sea ice zone: (a) difference between MLS and the sub-surface salinity maximum S_{\max} , (b) subsurface temperature maximum T_{\max} ($^{\circ}\text{C}$ above freezing), (c) depth of T_{\max} , and (d) the ratio of thermocline strength ΔT to halocline strength ΔS between the base of the ML and T_{\max} . The solid black line represents the mean winter sea ice edge.

most accessible in the eastern Pacific sector, across the Bellingshausen and Amundsen Seas. If an additional amount of winter ice growth equivalent to SD^* was to occur in this region, heat would be ventilated at a mean rate of $3\text{--}4 \times 10^6 \text{ J m}^{-2}$ per centimeter of ice growth. These values are 2–3 times lower in the Atlantic sector and northern Ross Sea. As discussed earlier, the mean ventilation efficiency given by γ_p would only be realized if the entire pycnocline is entrained into the ML. In

reality, most of the heat stored within the pycnocline is not accessible via sea ice-driven entrainment. This is especially the case in regions like the Bellingshausen Sea, where full pycnocline erosion would require an unrealistic amount of winter ice growth. Thus, γ_p gives a distorted view of the true wintertime ventilation efficiency.

A better measure of heat accessibility is given by γ [Eq. (8)], which quantifies the efficiency with which sea

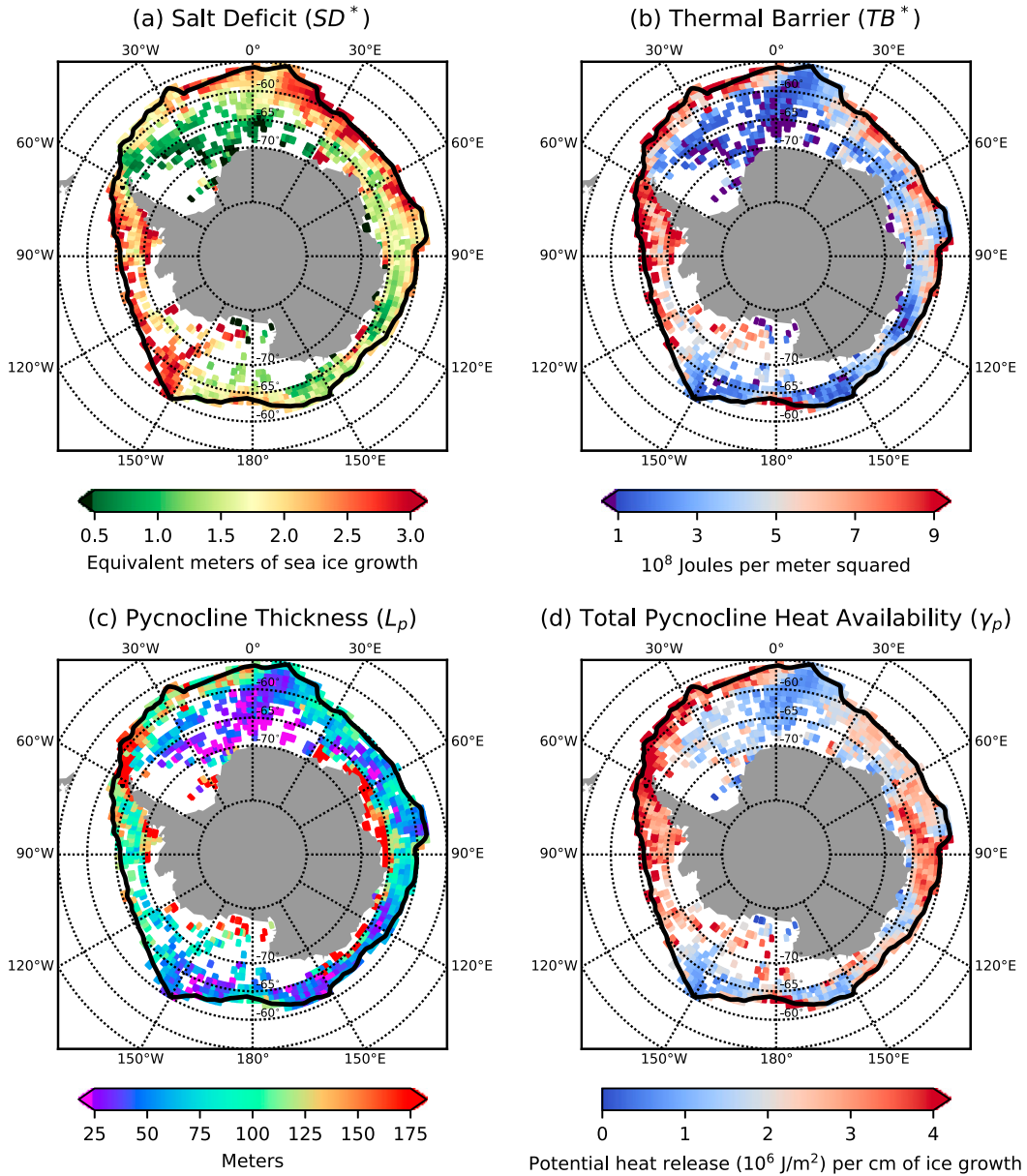


FIG. 7. Winter upper-ocean stability and heat availability within the winter sea ice zone: (a) pycnocline salt deficit (SD^*), (b) thermal barrier (TB^*), (c) pycnocline thickness L_p , and (d) total pycnocline heat availability $\gamma_p = TB^*/SD^*$. The solid black line represents the mean winter sea ice edge.

ice growth may ventilate heat down to an arbitrary depth. As the ML entrains the thermocline, each unit of ice growth will liberate an increasingly larger amount of heat. Therefore, γ is expected to have a strong depth dependence. This depth dependence is examined for four representative offshore regions: Mawson Sea, Bellingshausen Sea, northern Ross Sea, and Maud Rise (Fig. 8). Among these regions, Maud Rise has the highest wintertime ventilation efficiency. Here, 10 m of sea ice-driven entrainment would liberate heat at an

average rate of 1 MJ m^{-2} (10^6 J m^{-2}) per centimeter of ice growth. Equivalently, this amount of sea ice-driven entrainment would release enough heat to melt roughly 35% of the initial ice growth. Ventilation efficiency is slightly lower in the Mawson Sea, and significantly lower in the Bellingshausen and northern Ross Sea. In the latter region, a similar amount of entrainment would liberate heat at an average rate of 0.35 MJ m^{-2} per centimeter of ice growth. These regional efficiency rates increase for larger amounts of entrainment. With

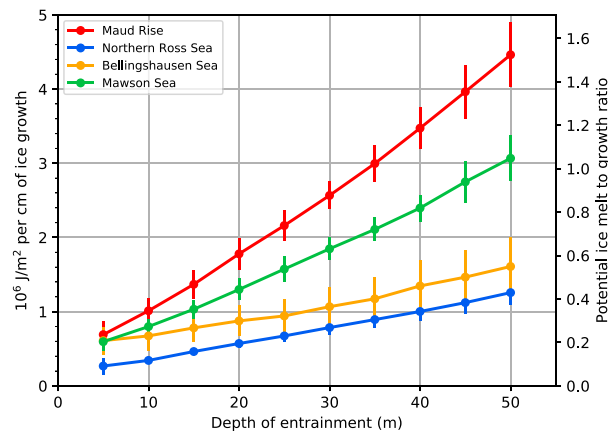


FIG. 8. Winter-mean ventilation efficiency, (8), over 50 m of entrainment for the northern Ross Sea, Bellingshausen Sea, Mawson Sea, and the Maud Rise region (see Fig. 1 for region boundaries). Vertical error bars represent one standard deviation.

30 m of sea ice–driven entrainment, the expected ventilation efficiency over Maud Rise is 2.5 MJ m^{-2} per centimeter of ice growth. In this scenario, enough heat would be ventilated to melt close to 90% of the initial ice growth.

From these results, we conclude that the Maud Rise region has an exceptionally strong negative feedback, or resistance, to winter sea ice growth. The strength of this feedback is expected to increase throughout the winter until ice growth is suppressed completely. This negative feedback is also relatively high in some regions along East Antarctica, but is notably lower in the Pacific sector. These results are consistent with the regional pattern obtained by comparing the strength of the thermocline to the strength of the corresponding halocline (Fig. 6d).

5. Simulations of winter ice–ocean coupling

The preceding observational analysis shows that the availability of thermocline heat varies greatly within the winter sea ice zone. The rate at which this sub-ML heat is ventilated will also depend on the atmospheric forcing. In principle, if the surface fluxes of buoyancy and momentum are known, one could accurately predict the ventilation rate for a given region. However, our ability to do so is greatly limited by the large uncertainties in the surface forcing, specifically the freshwater flux from sea ice. Here, this issue is sidestepped by addressing the related, but more tractable, question of how a given slab of sea ice will evolve in different ocean regions under uniform atmospheric forcing. This is done using an idealized, 1D sea ice–ocean model. The purpose of this exercise is not to accurately reproduce observations. Rather, our intent is to isolate and diagnose the

thermodynamic coupling between winter ice growth and ocean ventilation across the sea ice zone. In doing so, we aim to build intuition for how the ice–ocean system will respond to changes in ocean stratification and surface forcing on various time scales.

a. An idealized 1D ice–ocean model

1) UPPER OCEAN

To simulate vertical mixing in the upper ocean, we used a modified version of the Price–Weller–Pinkel (PWP) ML model (Price et al. 1986). Several studies have employed this model to simulate upper-ocean mixing in sea ice–covered regions (e.g., Hyatt 2006; Dewey et al. 2017; Biddle et al. 2017). In essence, this model parameterizes the vertical mixing that results from static and shear instabilities. Static instabilities are resolved using a convective adjustment scheme that mixes a statically unstable layer with progressively deeper layers until the entire profile becomes statically stable. Shear instabilities are assessed and resolved using bulk and gradient Richardson number stability criteria. Following other applications of the PWP model (e.g., Toole et al. 2010), a linear drag term is added to the momentum budget to crudely parameterize the momentum loss associated with the radiation of internal waves. This drag term has a decay time scale of 5 days, which is roughly 10 times greater than the local inertial period.

The PWP model is driven by surface fluxes of heat, freshwater, and momentum. The model uses a time interval of 6 h and a vertical resolution of 0.5 m (see Table 1). At each time step, the model applies surface fluxes to the ocean profile, then resolves any static or shear instabilities that are introduced. After the profile is stabilized, surface fluxes from the next time step are applied and the process is repeated.

2) THERMODYNAMIC SEA ICE

To simulate sea ice growth, we used a simplified version of the sea ice model introduced by Semtner (1976). This model treats snow and sea ice as homogeneous slabs with linear temperature profiles (Fig. 9). At the surface, the model is driven by the balance of upward and downward longwave radiation and the diffusion of heat through the snow and sea ice layers. The latter is determined using the thermal conductivities for snow and sea ice employed by Semtner (1976). Given our focus on the winter season, we assume that shortwave radiation and air–ice sensible and latent heat fluxes are negligibly small. Based on values obtained from ERA-Interim (Dee et al. 2011), we forced the model with a typical wintertime downward longwave heat flux of 200 W m^{-2} .

TABLE 1. Key parameters and constants used in the idealized 1D ice–ocean model.

Symbol	Description	Value
F_{dlw}	Downward longwave radiation	200 W m^{-2}
T_f	Freezing point of seawater	-1.86°C
κ_i	Thermal conductivity of sea ice	$2 \text{ W m}^{-1} \text{ K}^{-1}$
κ_s	Thermal conductivity of snow	$0.31 \text{ W m}^{-1} \text{ K}^{-1}$
ρ_0	Reference density of seawater	1027 kg m^{-3}
ρ_i	Density of sea ice	920 kg m^{-3}
ρ_a	Density of air	1.2 kg m^{-3}
c_h	Ocean–ice heat transfer coefficient	0.0056
c_w	Specific heat capacity of seawater	$4180 \text{ J kg}^{-1} \text{ K}^{-1}$
c_a	Specific heat capacity of air	$1000 \text{ J kg}^{-1} \text{ K}^{-1}$
L_i	Latent heat of fusion of ice	$3.3 \times 10^5 \text{ J kg}^{-1}$
S_i	Salinity of sea ice	4 psu
Δz	Vertical resolution of ocean model	0.5 m

At the base of the ice, accretion or ablation is governed by

$$\frac{dh_i}{dt} = \frac{1}{L_i \rho_i} (F_i - F_{oi}), \quad (9)$$

where h_i is ice thickness, F_i is the upward conductive heat flux through sea ice, and F_{oi} is the ocean–ice heat flux. The resulting change in the surface salinity of the ocean ΔS is given by

$$\Delta S = \frac{\Delta h_i}{\Delta z} (S_{z=0} - S_i), \quad (10)$$

where Δz is the thickness of the ocean surface layer, $S_{z=0}$ is surface ocean salinity, and S_i is a reference sea ice salinity.

To maintain focus on the coupling between ice growth and ocean ventilation, we ignore the effects of snow accumulation and the possibility of snow-ice formation. The latter is an alternate mode of ice formation that occurs when the weight of the snow layer depresses the ice surface below sea level (Eicken et al. 1995). The distinction between basal ice growth and snow-ice formation is of secondary importance to the ice–ocean feedbacks that are of interest in this study. Though the amount of brine may be significantly different, the ocean’s response will be fundamentally the same.

3) ICE–OCEAN COUPLING

The sea ice and ocean layers are thermodynamically coupled via an ocean–ice heat flux F_{oi} . Following McPhee (1992), F_{oi} is parameterized as

$$F_{oi} = c_w \rho_w c_h u^* (T_{z=0} - T_f), \quad (11)$$

where c_h is a turbulent heat exchange coefficient and u^* is the friction speed at the ice–ocean interface. Using the

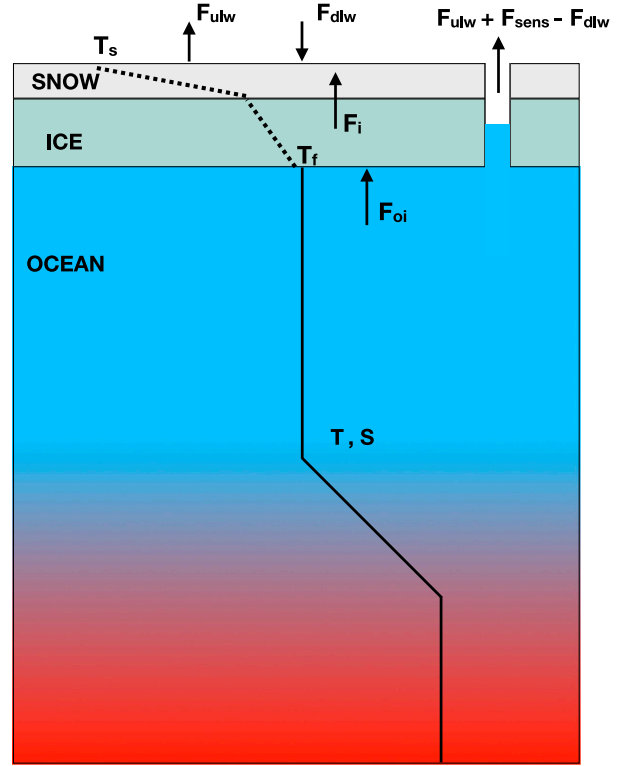


FIG. 9. Schematic showing the key processes represented in the idealized 1D thermodynamic ice–ocean model. The snow and ice layers are modeled following Semtner (1976). These layers are treated as single slabs with linear temperature profiles. Mixing within the ocean layer is simulated using the PWP upper-ocean model (Price et al. 1986). Parameters T_s and T_f represent the temperatures of the snow surface and ice base, respectively. F_{ulw} , F_{dlw} , F_i , F_{oi} , and F_{sens} are the heat fluxes due to upward longwave radiation, downward longwave radiation, conductive heat transfer through ice and snow, and sensible heat transfer, respectively. Key model parameters are listed in Table 1. Further details are provided in the text.

results from McPhee et al. (1999), we set c_h to be 0.0056. The friction speed u^* is equivalent to the square root of the kinematic ice–ocean stress, which is given by

$$u^* = (|\tau_{oi}|/\rho_w)^{1/2}. \quad (12)$$

The ice–ocean stress τ_{oi} is determined using the “rule of thumb” relationship proposed by Martinson and Wamser (1990), whereby τ_{oi} is assumed to be one-third the magnitude of the air–ice stress τ_{ai} , which is given by

$$\tau_{ai} = \rho_a C_{ai} U_0 \mathbf{u}, \quad (13)$$

where $C_{ai} = 2.36 \times 10^{-3}$ is the air–ice drag coefficient, ρ_a is the density of air, and \mathbf{u} is the near-surface wind velocity. The open-water fraction is set to a constant value of 0.05, which is typical for the winter sea ice

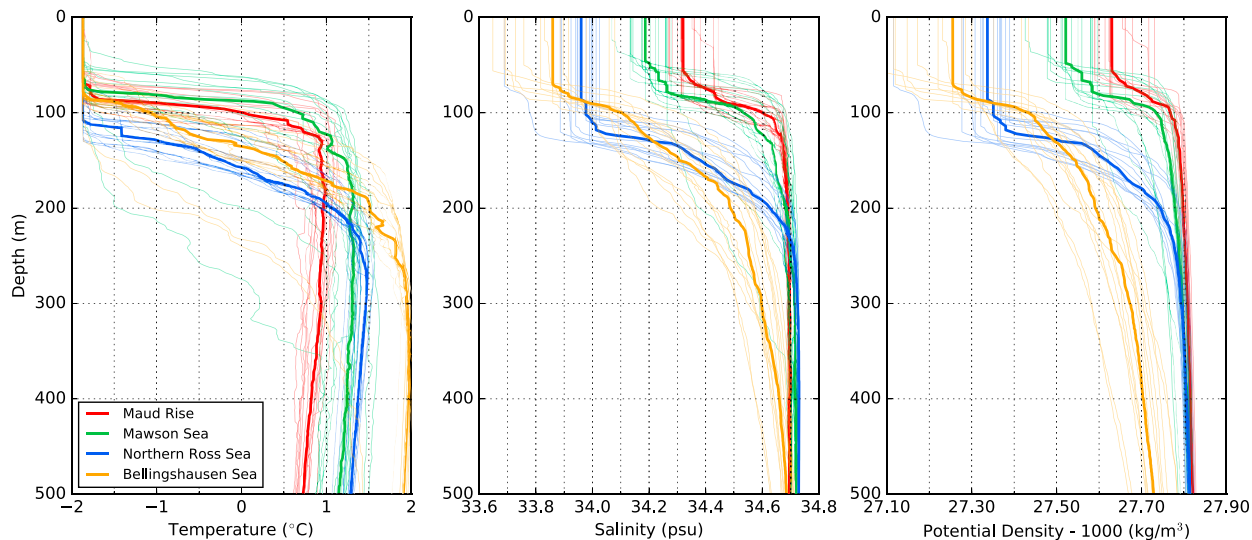


FIG. 10. Argo float profiles (thin lines) from June that are used to initialize the idealized 1D model simulations, color coded by region (see Fig. 1 for region boundaries). As a visual aid, the median profile for each region (thick lines) is shown.

zone. Given this assumption of near total winter sea ice cover, we take τ_{oi} as an approximate value for the total stress applied to the ocean surface.

4) OCEAN HEAT LOSS THROUGH LEADS

Since the sea ice and snow layers effectively insulate the ocean, a disproportionate amount of ocean heat is lost through leads. For simplicity, we only consider the heat losses that occur via blackbody longwave radiation and sensible heat fluxes F_{sens} . The former is partially offset by the prescribed downward longwave heat flux described earlier. The latter is estimated using the simple bulk formula described by Friehe et al. (1976):

$$F_{sens} = (1 - \alpha)\rho_a c_a C_H U_0 \Delta T_a, \quad (14)$$

where α is the sea ice area fraction, c_a is the heat capacity of air, U_0 is the near-surface wind speed, ΔT_a is the air–sea temperature difference, and $C_H = 1 \times 10^{-3}$ is the bulk transfer coefficient for sensible heat. Without an atmospheric model to determine T_a , we simply assume a typical wintertime air–sea temperature difference of 20°C.

5) INITIAL CONDITIONS AND SURFACE FORCING

Model runs were initialized using ensembles of early winter Argo float profiles from the northern Ross Sea, Maud Rise, Bellingshausen Sea, and Mawson Sea (Fig. 10). These regions were chosen because they span the observed range of upper-ocean stratification and heat availability across the offshore regions of the winter sea ice zone (Fig. 7). From each region, we randomly selected 15 float profiles collected in the month of June,

and used each profile to initialize a model simulation. Each initial profile was then forced with identical surface conditions for 120 days, thereby simulating one full winter season. For our control forcing, we constructed an artificial time series of surface winds that replicate moderate winter conditions in the sea ice zone (Fig. 11). This was done using the Markov method described by (29) in Bretherton et al. (1992), which produces a red noise sequence from a randomly generated white noise sequence. These synthetic winds have a standard deviation of 5 m s^{-1} and a (6 hourly) lag-1 autocorrelation of 0.9. This autocorrelation was estimated from gridpoint estimates of 10-m wind velocity for the Weddell Sea region from ERA-Interim (Dee et al. 2011). A similar approach could be used to construct an artificial time series for the downward longwave radiation. However, we find that doing so does not fundamentally alter our main results.

Each run is initialized with 30 cm of sea ice and 5 cm of snow, which are typical early winter values for the region (Worby et al. 2008). Sea ice thickness was allowed to evolve, but snow depth and sea ice fraction were kept constant.

b. Model results

1) CONTROL EXPERIMENT WITH MODERATE WINDS

Results from the control experiment demonstrate that the thermohaline structure of the upper ocean significantly influences winter sea ice growth in the Southern Ocean (Fig. 12). Sea ice growth in runs initialized with profiles from the strongly stratified northern Ross Sea

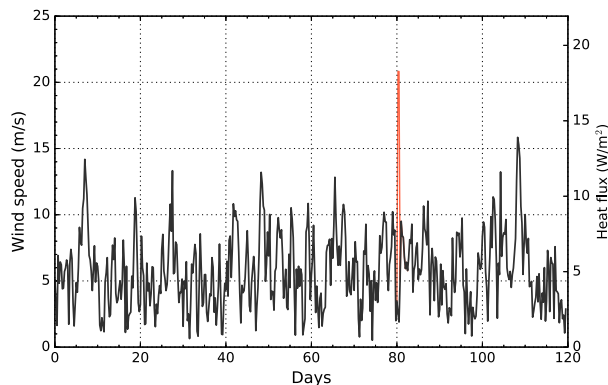


FIG. 11. The artificially generated time series of wind speed that is applied to the profiles shown in Fig. 10. The black line represents the control forcing that replicates moderate winds in the winter sea ice zone. The red line highlights the storm perturbation. The ocean–air sensible heat flux is given by (14) and is scaled by the open water fraction (0.05).

was weakly affected by the entrainment of heat into the ML. In these runs, sea ice grew continuously throughout the winter and reached a median thickness that is similar to that produced in the absence of ocean heat fluxes (dashed line). At the other extreme, ice growth was heavily suppressed in the Maud Rise simulations, with the eventual net ice growth being 50% less than the case without ocean heat fluxes. The Maud Rise runs also featured the highest rates of ocean heat loss (Fig. 12b). After day 40 when sea ice thickness in the Maud Rise simulations began to plateau, the corresponding ocean heat flux mostly varied between 20 and 50 W m^{-2} . Despite the idealized nature of these experiments, this range of winter ocean heat loss agrees well with observations (e.g., McPhee et al. 1999). In contrast, the ocean heat flux for the northern Ross Sea simulations varied between 10 and 20 W m^{-2} .

The evolution of MLS mirrors that of sea ice thickness (Fig. 12d). For the latter half of the Maud Rise simulations, less than 20 cm of additional sea ice growth would have guaranteed the full erosion of the pycnocline (Fig. 12a). However, this amount of sea ice growth was never realized, as the entrainment heat flux eventually grew to balance the heat loss at the surface. In general, MLD steadily increased throughout each simulation (Fig. 12e). However, in a few of the Maud Rise ensemble members, fluctuations in the ocean heat flux led to brief periods of ice melt and ML shoaling (not shown).

These idealized experiments were repeated using different values for initial sea ice and snow-layer thicknesses ranging from 25 to 75 cm and from 5 to 15 cm, respectively. Results from those experiments are qualitatively similar to the case presented here. These results are also not sensitive to modest changes to the open-water

fraction and surface air temperature. However, we do note that the results for the Maud Rise simulations are somewhat sensitive to the vertical resolution of the ocean model. Choosing a vertical resolution coarser than 5 m produces a notable increase in the variability of the ocean–ice heat flux and leads to more frequent episodes of ice melt. This is the case since a coarser vertical resolution causes entrainment to occur in larger steps.

2) STORM PERTURBATION EXPERIMENTS

When forced with moderate winds, the Maud Rise ice–ocean system evolves to a state in which the ocean–ice heat fluxes approximately balance the conductive heat flux through the ice. To test the sensitivity of this late winter equilibrium, the previous experiment was repeated with the addition of a storm on day 80 (red line in Fig. 11). During this perturbation period, a maximum wind speed of approximately 21 m s^{-1} ($\sim 40 \text{ kt}$; $1 \text{ kt} \approx 0.51 \text{ m s}^{-1}$) was imposed for 12 h. This wind event is similar in magnitude to strong winter storms observed in the Weddell (e.g., McPhee et al. 1996).

For the Maud Rise simulations, the introduction of this storm triggered an abrupt increase in MLT (Fig. 13). This resulted from the enhanced shear-driven entrainment associated with the large input of momentum at the ocean surface. This warming, coupled with the increase in u^* , amplified the ocean–ice heat flux. The magnitude of the ocean heat loss varied greatly among the ensemble members, ranging from 50 to 200 W m^{-2} . In response, sea ice thinned by 5–20 cm and created a shallow meltwater layer that persisted for several days. In the other regional simulations, the impact of the storm ranged from weak to negligible. Introducing the storm at a different time, in the latter half of the simulation, produces results that are qualitatively similar to those described here. However, we note that the amplitude of the ocean response in the Maud Rise simulations is somewhat sensitive to the timing of the storm.

From these results, we can infer circumstances that may lead to greater melt or even the complete elimination of the winter ice layer. First, it is evident that a weaker pycnocline promotes thinner sea ice and a stronger response to wind events. Additionally, since the impact of wind-driven mixing diminishes with depth, a shoaling of the thermocline would also favor higher ventilation rates. Last, a simple increase in the frequency of winter storms would also increase the likelihood of major wintertime melt events.

To demonstrate the compounding effects of these processes, the previous experiment was repeated with two modifications. First, the initial profiles were shifted upward by 25 m. This was done by truncating the ML. For comparison, Gordon and Huber (1990) estimate an upwelling rate of 45 m yr^{-1} across the Weddell region.

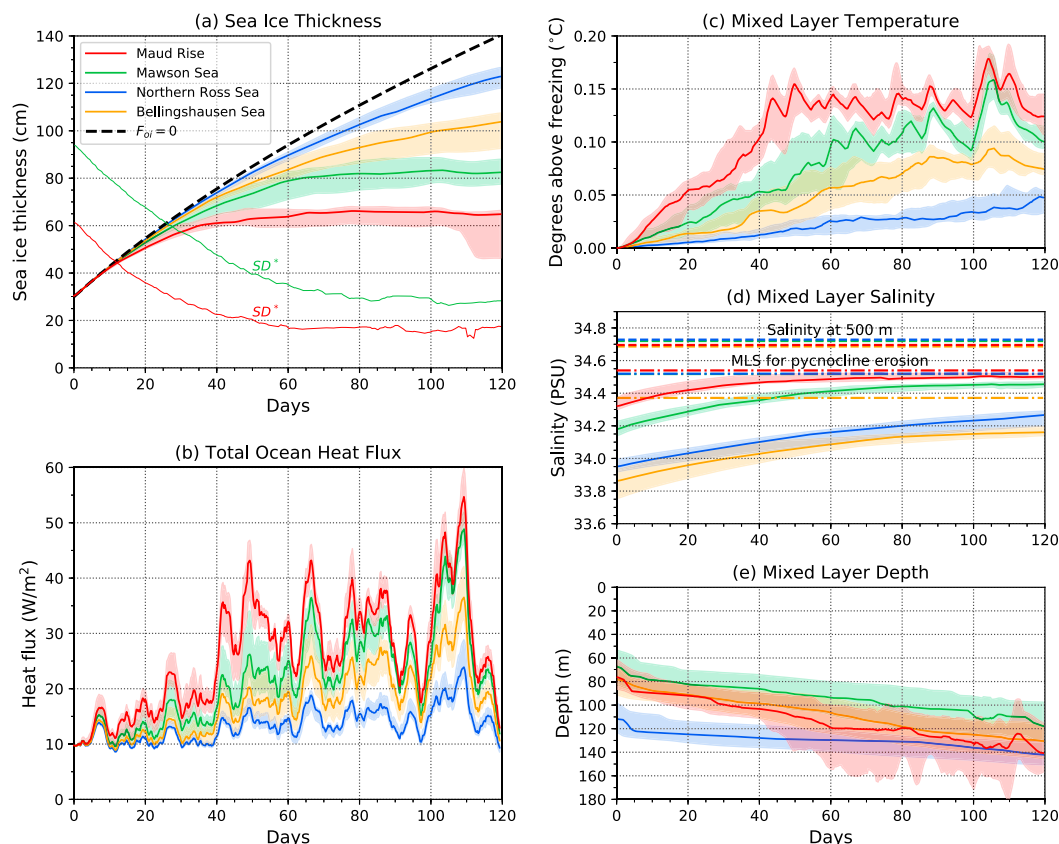


FIG. 12. Simulations of sea ice thickness and upper-ocean properties using the control forcing: (a) sea ice thickness, (b) ocean heat loss, (c) MLT, (d) MLS, and (e) MLD. The solid lines and shading represent the median value and interquartile range (25th–75th percentiles) for each regional ensemble, respectively. In (a), the dashed black line represents the evolution of sea ice in the absence of ocean heat fluxes and the thin lines show the pycnocline salt deficit (SD^*). SD^* for the Bellingshausen Sea and northern Ross Sea exceeds the range of sea ice thickness shown in (a). In (d), the dashed lines represent salinity at 500 m, while the dashed–dotted lines represent the MLS required for full pycnocline erosion. Each time series has been smoothed with a 2-day running-mean filter.

Additionally, a second storm, identical to the first, was added on day 85. The shoaling of the thermocline led to stronger suppression of ice growth (Fig. 14). For the Maud Rise and Mawson Sea simulations, this is evident in the days leading up to the storm events. In the Maud Rise runs, the storm events triggered an extended period of exceptionally high ocean heat loss and a dramatic change in sea ice thickness, which declined to 10–50 cm across simulations following the storm. As before, the magnitude of this response varied greatly among the regional ensemble members. This extreme perturbation produced a similar but more muted response in the Mawson Sea simulations. However, the ice–ocean system in the other regional simulations remained largely unaffected.

6. Summary and conclusions

In this study, we have analyzed the thermodynamic coupling between winter sea ice growth and upper-ocean

stratification in the Southern Ocean. Part of this effort involved quantifying the upper ocean’s susceptibility to deep convection and the accessibility of heat below the ML. To this end, we have developed modified versions of the bulk stability metrics introduced by M90 and M98. These metrics were evaluated for the entire winter sea ice zone using observed under-ice CTD profiles, mainly from Argo floats and instrumented seals. This analysis reveals a contrasting pattern of upper-ocean stability across the Atlantic and Pacific Ocean sectors. In the latter region, specifically the offshore regions of the Bellingshausen and Amundsen Seas, the additional winter sea ice growth that is needed to fully erode the pycnocline, as quantified by SD^* , is several times larger than the sea ice growth that normally occurs in a single winter season. This indicates that offshore wintertime deep convection is extremely unlikely to occur in these areas. In the Atlantic sector, in particular near the Maud Rise seamount, SD is comparable to the total amount of

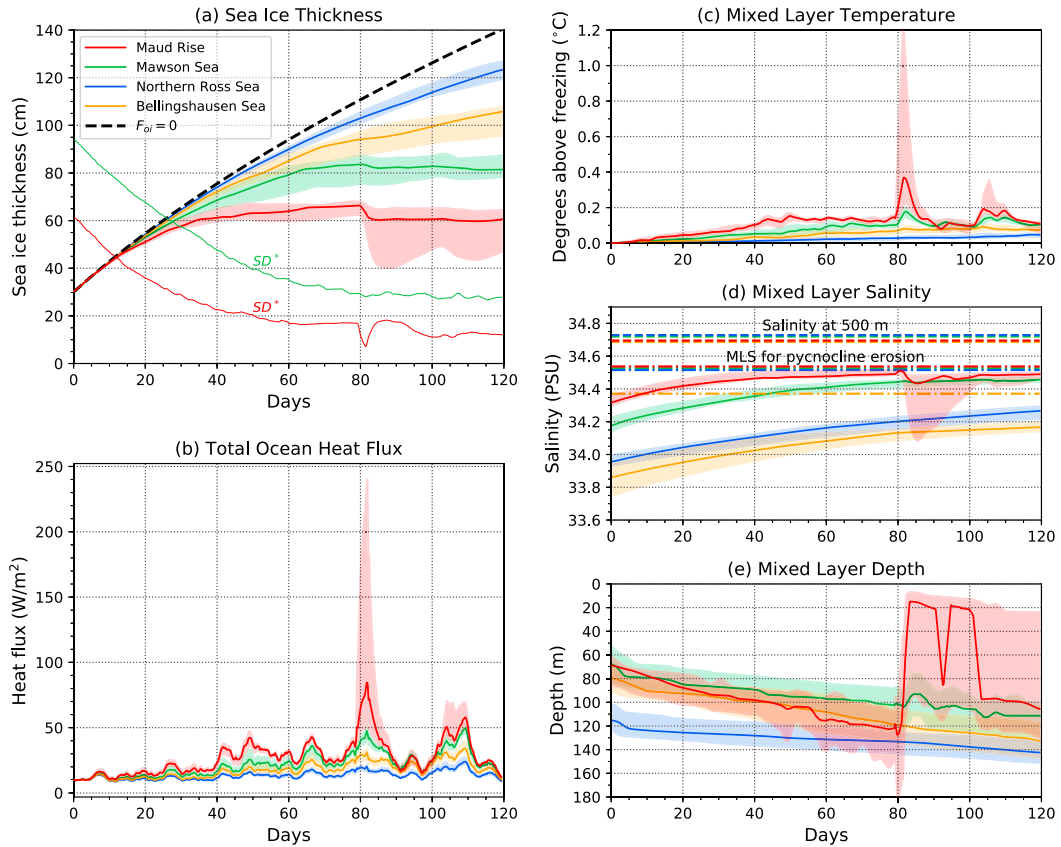


FIG. 13. As in Fig. 12, but for the storm perturbation forcing shown in Fig. 11.

ice growth that occurs in a winter season. Given that the computation of SD neglects multiple non-ice-related processes that may erode the pycnocline, such as wind-driven mixing, these observations suggest that large swaths of the Weddell region are somewhat vulnerable to wintertime deep convection. However, the weak pycnocline in these regions also support a relatively sharp thermocline. This combination of weak stratification and large sub-ML temperature gradient favors a high rate of wintertime heat ventilation and a strong negative feedback to ice growth. More generally, the off-shelf regions across the southern Atlantic sector and along the East Antarctic shelf break are characterized by relatively high ventilation efficiency. Thus, a given amount of winter sea ice growth in these regions will ventilate more heat compared to elsewhere in the sea ice zone.

This observational assessment is supported by results from idealized experiments conducted with a 1D sea-ice-ocean model. In our control simulations, which featured moderate wind conditions, simulations initialized with profiles from the Maud Rise region evolved to a state in which ocean-ice heat fluxes approximately balanced the atmospheric cooling imposed at the sea ice surface. This

balance was maintained over the latter half of winter, during which sea ice thickness was approximately constant. At the other extreme, sea ice growth in simulations initialized with profiles from the northern Ross Sea was largely unaffected by the comparatively small entrainment of heat into the ML. From the latter result, we speculate that ice growth in similarly strongly stratified regions near the winter sea ice edge are also weakly affected by the entrainment of heat from the thermocline.

The Maud Rise simulations provide a clear example of the winter ice-ocean feedback mechanism envisioned by M90. Even though the Maud Rise water column is seemingly susceptible to deep convection, the heat entrained into the ML is able to suppress ice growth and limit further erosion of the pycnocline. Additional model experiments show that the surface stress imparted by a typical 1-day storm event can disrupt this balance and cause substantial ice melt. The magnitude of the ocean response is critically dependent on the stratification of the water column at the moment the storm is applied. For the Maud Rise simulations, the ensuing rate of ocean heat loss was 2–3 times higher than in the case with moderate winds. This response can be greatly amplified by strong upwelling, which exposes the

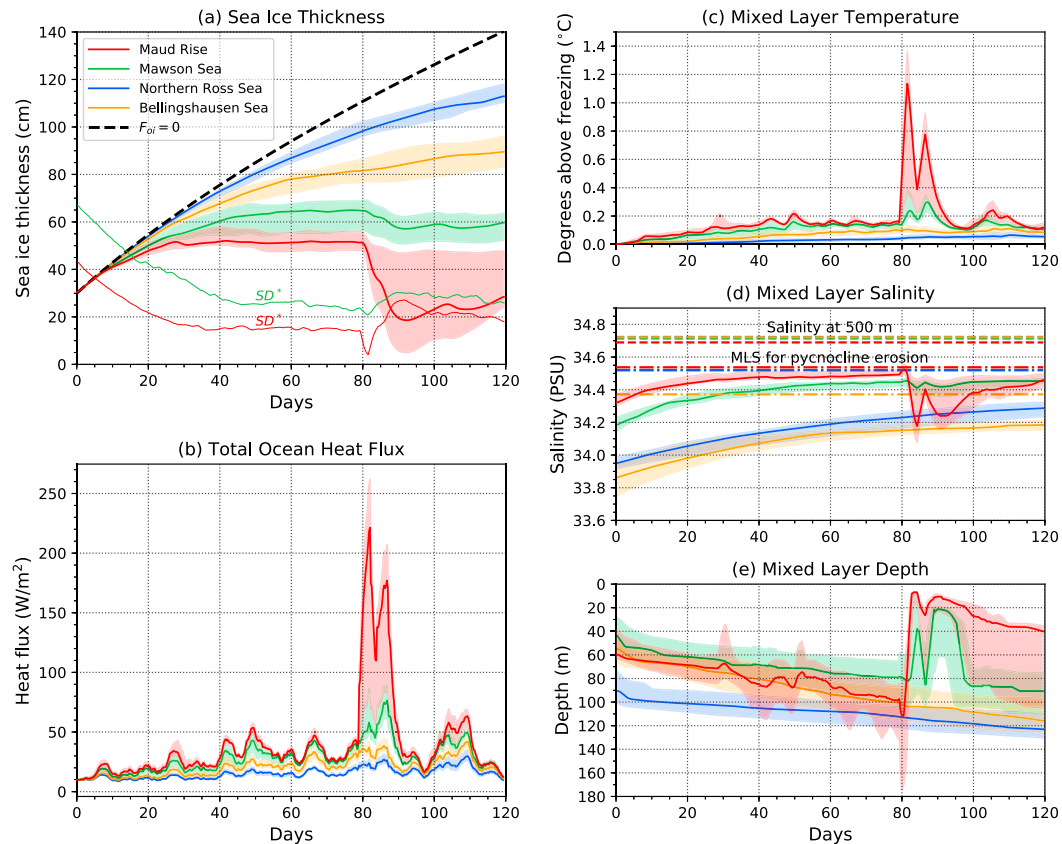


FIG. 14. As in Fig. 13, but with the initial profiles shifted upward by 25 m and a second identical storm added on day 85.

thermocline to more intense wind-driven mixing. In the other regional simulations, which featured stronger stratification, the storm had a weak effect on ventilation rates. These results suggest that the cumulative wintertime ventilation of the deep ocean heat in weakly stratified regions is dominated by short-lived storm events. Examples of such events were documented during the ANZFLUX survey of the Maud Rise region during the winter of 1994 (McPhee et al. 1996, 1999). In one case, the passing of a powerful storm, which featured gusts up to 25 m s^{-1} , produced ocean heat fluxes that exceeded 100 W m^{-2} . This was several times larger than the mean heat flux measured over the 6-week survey.

Given our results, we hypothesize that a series of exceptionally strong storms, acting on a shoaled pycnocline that is sufficiently weak, could release enough heat to completely melt the winter ice cover. This assertion is consistent with the tendency for transient winter polynyas to appear along the flanks of Maud Rise, where the stratification is weak and thermocline is consistently shallow (Comiso and Gordon 1987; Lindsay et al. 2008; de Steur et al. 2007). This conjecture also agrees with past studies that have linked the appearance of

winter polynyas to enhanced upwelling across the Weddell Gyre (e.g., Lemke 1987; Hirabara et al. 2012; Cheon et al. 2015; Kurtakoti et al. 2018). Given that these oceanic preconditions are important, we emphasize a storm's unique capacity to rapidly ventilate large amounts of heat. Without such an abrupt perturbation, heat fluxes from the thermocline will tend to maintain a thin sea ice cover that undergoes cycles of partial melt and regrowth throughout the winter. This proposed mechanism also complements existing theories that describe how topography–flow interactions over Maud Rise elevate isopycnals along the flanks of the seamount and produce low sea ice concentration in specific areas (e.g., Holland 2000). The dynamics that arise from these topographical interactions will modulate the evolution of a polynya after it is formed. Though not explored in this study, we speculate that strong surface divergence would further amplify the impact of a storm by advecting ice and meltwater away from the affected region. This mechanism would undermine the restratification of the upper ocean and intensify the surface cooling that drives thermal convection.

With these insights, we acknowledge the idealized nature of our theoretical framework. One important process that is neglected here is the accumulation of snow, which reduces basal ice growth over the course of winter. This process may play a more important role in limiting ice growth in regions where the wintertime entrainment heat flux is low. Additionally, our analysis does not account for many 3D processes that can modulate local ocean stratification, ice thickness, and ice areal fraction. Nevertheless, our results can serve as a basis for future work that explores these additional processes in more detail.

Our results indicate that changes to upper-ocean salinity will have far-reaching impacts on the regional ice-ocean system. Recent studies have linked the freshening of the Southern Ocean to a buildup of deep ocean heat within the sea ice zone (Goosse and Zunz 2014; Lecomte et al. 2017). Our findings support this relationship, with the added caveat that regions with large sub-ML heat availability or high rates of sea ice growth will have greater sensitivity to changes in surface salinity. Other studies have suggested that this freshening trend will lead to fewer winter polynyas (e.g., Gordon et al. 2007; de Lavergne et al. 2014). Our results also support this projection, but we caution that changes in the wind forcing, which may lead to stronger upwelling or more frequent winter storms, may counter the effect of this freshening. Last, this study endorses recent efforts to highlight the coupling between winter sea ice growth and ML entrainment as an important feedback in the Southern Ocean climate system (e.g., Goosse et al. 2018). That stated, our results demonstrate that spatiotemporal variations in stratification exert strong control on the strength of this feedback. More observations and detailed modeling will be needed to properly characterize the variability of this feedback and its susceptibility to future change.

Acknowledgments. E. W., S. R., and A. W. gratefully acknowledge financial support from the National Science Foundation and the National Oceanic and Atmospheric Administration through Grants OPP-1429342 and NA15OAR4320063, respectively. E. C. acknowledges funding from the University of Washington Program in Climate Change, ARCS Foundation, and National Defense Science and Engineering Graduate Fellowship (NDSEG) Program. The Argo float data were primarily collected and made freely available by the International Argo Program and the national programs that contribute to it (<http://www.argo.ucsd.edu>, <http://argo.jcommops.org>). The Argo Program is part of the Global Ocean Observing System. Additional float data were collected and made freely available by the Southern Ocean Carbon and Climate

Observations and Modeling (SOCCOM) project funded by the National Science Foundation, Division of Polar Programs (NSF PLR-1425989). The marine mammal data were collected and made freely available by the International MEOP Consortium and the national programs that contribute to it (<http://www.meop.net>). Two anonymous reviewers provided helpful feedback that greatly improved this manuscript.

REFERENCES

- Akitomo, K., 1999: Open-ocean deep convection due to thermobaricity: 1. Scaling argument. *J. Geophys. Res.*, **104**, 5225–5234, <https://doi.org/10.1029/1998JC900058>.
- Argo, 2018: Argo float data and metadata from Global Data Assembly Centre (Argo GDAC)—Snapshot of Argo GDAC as of 8 March 2018. SEANOE, accessed 3 March 2018, <https://doi.org/10.17882/42182#55429>.
- Biddle, L. C., K. J. Heywood, J. Kaiser, and A. Jenkins, 2017: Glacial meltwater identification in the Amundsen Sea. *J. Phys. Oceanogr.*, **47**, 933–954, <https://doi.org/10.1175/JPO-D-16-0221.1>.
- Boehme, L., P. Lovell, M. Biuw, F. Roquet, J. Nicholson, S. E. Thorpe, M. P. Meredith, and M. Fedak, 2009: Technical note: Animal-borne CTD-satellite relay data loggers for real-time oceanographic data collection. *Ocean Sci.*, **5**, 685–695, <https://doi.org/10.5194/os-5-685-2009>.
- Bretherton, C. S., C. Smith, and J. M. Wallace, 1992: An intercomparison of methods for finding coupled patterns in climate data. *J. Climate*, **5**, 541–560, [https://doi.org/10.1175/1520-0442\(1992\)005<0541:AIOMFF>2.0.CO;2](https://doi.org/10.1175/1520-0442(1992)005<0541:AIOMFF>2.0.CO;2).
- Charrassin, J.-B., and Coauthors, 2008: Southern Ocean frontal structure and sea-ice formation rates revealed by elephant seals. *Proc. Natl. Acad. Sci. USA*, **105**, 11 634–11 639, <https://doi.org/10.1073/pnas.0800790105>.
- Cheon, W. G., S. K. Lee, A. L. Gordon, Y. Liu, C. B. Cho, and J. J. Park, 2015: Replicating the 1970s' Weddell Polynya using a coupled ocean-sea ice model with reanalysis surface flux fields. *Geophys. Res. Lett.*, **42**, 5411–5418, <https://doi.org/10.1002/2015GL064364>.
- Comiso, J. C., and A. L. Gordon, 1987: Recurring polynyas over the Cosmonaut Sea and the Maud Rise. *J. Geophys. Res.*, **92**, 2819–2833, <https://doi.org/10.1029/JC092iC03p02819>.
- Dee, D. P., and Coauthors, 2011: The ERA-Interim reanalysis: Configuration and performance of the data assimilation system. *Quart. J. Roy. Meteor. Soc.*, **137**, 553–597, <https://doi.org/10.1002/qj.828>.
- de Lavergne, C., J. B. Palter, E. D. Galbraith, R. Bernardello, and I. Marinov, 2014: Cessation of deep convection in the open Southern Ocean under anthropogenic climate change. *Nat. Climate Change*, **4**, 278–282, <https://doi.org/10.1038/nclimate2132>.
- de Stuur, L., D. M. Holland, R. D. Muench, and M. G. McPhee, 2007: The warm-water “Halo” around Maud Rise: Properties, dynamics and impact. *Deep-Sea Res. I*, **54**, 871–896, <https://doi.org/10.1016/j.dsr.2007.03.009>.
- Dewey, S. R., J. H. Morison, and J. Zhang, 2017: An edge-referenced surface fresh layer in the Beaufort Sea seasonal ice zone. *J. Phys. Oceanogr.*, **47**, 1125–1144, <https://doi.org/10.1175/JPO-D-16-0158.1>.
- Drucker, R., S. Martin, and R. Kwok, 2011: Sea ice production and export from coastal polynyas in the Weddell and Ross

- Seas. *Geophys. Res. Lett.*, **38**, L17502, <https://doi.org/10.1029/2011GL048668>.
- Eicken, H., H. Fischer, and P. Lemke, 1995: Effects of the snow cover on Antarctic sea ice and potential modulation of its response to climate change. *Ann. Glaciol.*, **21**, 369–376, <https://doi.org/10.1017/S0260305500016086>.
- Fahrbach, E., G. Rohardt, M. Schröder, and V. Strass, 1994: Transport and structure of the Weddell Gyre. *Ann. Geophys.*, **12**, 840–855, <https://doi.org/10.1007/s00585-994-0840-7>.
- Foster, T. D., and E. C. Carmack, 1976: Temperature and salinity structure in the Weddell Sea. *J. Phys. Oceanogr.*, **6**, 36–44, [https://doi.org/10.1175/1520-0485\(1976\)006<0036:TASSIT>2.0.CO;2](https://doi.org/10.1175/1520-0485(1976)006<0036:TASSIT>2.0.CO;2).
- Friehe, C. A., K. F. Schmitt, C. A. Friehe, and K. F. Schmitt, 1976: Parameterization of air–sea interface fluxes of sensible heat and moisture by the bulk aerodynamic formulas. *J. Phys. Oceanogr.*, **6**, 801–809, [https://doi.org/10.1175/1520-0485\(1976\)006<0801:POASIF>2.0.CO;2](https://doi.org/10.1175/1520-0485(1976)006<0801:POASIF>2.0.CO;2).
- Gill, A. E., 1973: Circulation and bottom water production in the Weddell Sea. *Deep-Sea Res. Oceanogr. Abstr.*, **20**, 111–140, [https://doi.org/10.1016/0011-7471\(73\)90048-X](https://doi.org/10.1016/0011-7471(73)90048-X).
- Goosse, H., and V. Zunz, 2014: Decadal trends in the Antarctic sea ice extent ultimately controlled by ice-ocean feedback. *Cryosphere*, **8**, 453–470, <https://doi.org/10.5194/tc-8-453-2014>.
- , and Coauthors, 2018: Quantifying climate feedbacks in polar regions. *Nat. Commun.*, **9**, 1919, <https://doi.org/10.1038/s41467-018-04173-0>.
- Gordon, A. L., 1978: Deep Antarctic convection west of Maud Rise. *J. Phys. Oceanogr.*, **8**, 600–612, [https://doi.org/10.1175/1520-0485\(1978\)008<0600:DACWOM>2.0.CO;2](https://doi.org/10.1175/1520-0485(1978)008<0600:DACWOM>2.0.CO;2).
- , and B. A. Huber, 1984: Thermohaline stratification below the Southern Ocean sea ice. *J. Geophys. Res.*, **89**, 641–648, <https://doi.org/10.1029/JC089iC01p00641>.
- , and —, 1990: Southern Ocean winter mixed layer. *J. Geophys. Res.*, **95**, 11 655–11 672, <https://doi.org/10.1029/JC095iC07p11655>.
- , C. T. Chen, and W. G. Metcalf, 1984: Winter mixed layer entrainment of Weddell Deep Water. *J. Geophys. Res.*, **89**, 637–640, <https://doi.org/10.1029/JC089iC01p00637>.
- , M. Visbeck, and J. C. Comiso, 2007: A possible link between the Weddell Polynya and the southern annular mode. *J. Climate*, **20**, 2558–2571, <https://doi.org/10.1175/JCLI4046.1>.
- Haumann, F. A., N. Gruber, M. Münnich, I. Frenger, and S. Kern, 2016: Sea-ice transport driving Southern Ocean salinity and its recent trends. *Nature*, **537**, 89–92, <https://doi.org/10.1038/nature19101>.
- Hirabara, M., H. Tsujino, H. Nakano, and G. Yamanaka, 2012: Formation mechanism of the Weddell Sea Polynya and the impact on the global abyssal ocean. *J. Oceanogr.*, **68**, 771–796, <https://doi.org/10.1007/s10872-012-0139-3>.
- Holland, D. M., 2000: Transient sea-ice polynya forced by oceanic flow variability. *Prog. Oceanogr.*, **48**, 403–460, [https://doi.org/10.1016/S0079-6611\(01\)00010-6](https://doi.org/10.1016/S0079-6611(01)00010-6).
- Hyatt, J., 2006: Wind, sea ice, inertial oscillations and upper ocean mixing in Marguerite Bay, Western Antarctic Peninsula: Observations and modeling. Ph.D. thesis, MIT/WHOI Joint Program, 168 pp., <https://doi.org/10.1575/1912/1238>.
- Jacobs, S. S., R. G. Fairbanks, and Y. G. Horibe, 1985: Origin and evolution of water masses near the Antarctic continental margin: Evidence from $H_2^{18}O/H_2^{16}O$ ratios in seawater. *Oceanology of the Antarctic Continental Shelf*, S. S. Jacobs, Ed., Antarctic Research Series, Vol. 43, Amer. Geophys. Union, 59–85.
- Johnson, G. C., 2008: Quantifying Antarctic Bottom Water and North Atlantic Deep Water volumes. *J. Geophys. Res.*, **113**, C05027, <https://doi.org/10.1029/2007JC004477>.
- Klatt, O., O. Boebel, and E. Fahrbach, 2007: A profiling float's sense of ice. *J. Atmos. Oceanic Technol.*, **24**, 1301–1308, <https://doi.org/10.1175/JTECH2026.1>.
- Kurtakoti, P., M. Veneziani, A. Stössel, and W. Weijer, 2018: Preconditioning and formation of maud rise polynyas in a high-resolution earth system model. *J. Climate*, **31**, 9659–9678, <https://doi.org/10.1175/JCLI-D-18-0392.1>.
- Kurtz, N. T., and T. Markus, 2012: Satellite observations of Antarctic sea ice thickness and volume. *J. Geophys. Res.*, **117**, C08025, <https://doi.org/10.1029/2012JC008141>.
- Lecomte, O., H. Goosse, T. Fichefet, C. De Lavergne, A. Barthélemy, and V. Zunz, 2017: Vertical ocean heat redistribution sustaining sea-ice concentration trends in the Ross Sea. *Nat. Commun.*, **8**, 258, <https://doi.org/10.1038/s41467-017-00347-4>.
- Lemke, P., 1987: A coupled one-dimensional sea ice-ocean model. *J. Geophys. Res.*, **92**, 13 164–13 172, <https://doi.org/10.1029/JC092iC12p13164>.
- Lindsay, R. W., R. Kwok, L. de Steur, and W. Meier, 2008: Halo of ice deformation observed over the Maud Rise seamount. *Geophys. Res. Lett.*, **35**, L15501, <https://doi.org/10.1029/2008GL034629>.
- Martinson, D. G., 1990: Evolution of the southern ocean winter mixed layer and sea ice: Open ocean deepwater formation and ventilation. *J. Geophys. Res.*, **95**, 11 641–11 654, <https://doi.org/10.1029/JC095iC07p11641>.
- , and C. Wamser, 1990: Ice drift and momentum exchange in winter Antarctic pack ice. *J. Geophys. Res.*, **95**, 1741–1755, <https://doi.org/10.1029/JC095iC02p01741>.
- , and R. A. Iannuzzi, 1998: Antarctic ocean-ice interaction: Implications from ocean bulk property distributions in the Weddell gyre. *Antarctic Sea Ice: Physical Processes, Interactions and Variability*, M. O. Jeffries, Ed., Antarctic Research Series, Vol. 74, Amer. Geophys. Union, 243–271.
- McDougall, T. J., and P. Barker, 2011: Getting started with TEOS-10 and the Gibbs Seawater (GSW) Oceanographic Toolbox. SCOR/IAPSO WG127, 28 pp., http://www.teos-10.org/pubs/Getting_Started.pdf.
- McPhee, M. G., 1992: Turbulent heat flux in the upper ocean under sea ice. *J. Geophys. Res.*, **97**, 5365–5379, <https://doi.org/10.1029/92JC00239>.
- , and D. G. Martinson, 1994: Turbulent mixing under drifting pack ice in the Weddell Sea. *Science*, **263**, 218–221, <https://doi.org/10.1126/science.263.5144.218>.
- , and Coauthors, 1996: The Antarctic Zone Flux Experiment. *Bull. Amer. Meteor. Soc.*, **77**, 1221–1232, [https://doi.org/10.1175/1520-0477\(1996\)077<1221:TAFZE>2.0.CO;2](https://doi.org/10.1175/1520-0477(1996)077<1221:TAFZE>2.0.CO;2).
- , C. Kottmeier, and J. H. Morison, 1999: Ocean heat flux in the central Weddell Sea during winter. *J. Phys. Oceanogr.*, **29**, 1166–1179, [https://doi.org/10.1175/1520-0485\(1999\)029<1166:OHFITC>2.0.CO;2](https://doi.org/10.1175/1520-0485(1999)029<1166:OHFITC>2.0.CO;2).
- Meier, W., F. Fetterer, M. Savoie, S. Mallory, R. Duerr, and J. Stroeve, 2017: NOAA/NSIDC climate data record of passive microwave sea ice concentration, version 3. National Snow and Ice Data Center, accessed 10 May 2018, <https://doi.org/10.7265/N59P2ZTG>.
- Muench, R. D., H. J. S. Fernando, and G. R. Stegen, 1990: Temperature and salinity staircases in the northwestern Weddell

- Sea. *J. Phys. Oceanogr.*, **20**, 295–306, [https://doi.org/10.1175/1520-0485\(1990\)020<0295:TASSIT>2.0.CO;2](https://doi.org/10.1175/1520-0485(1990)020<0295:TASSIT>2.0.CO;2).
- Pellichero, V., J. B. Sallée, S. Schmidtke, F. Roquet, and J. B. Charrassin, 2017: The ocean mixed layer under Southern Ocean sea-ice: Seasonal cycle and forcing. *J. Geophys. Res. Oceans*, **122**, 1608–1633, <https://doi.org/10.1002/2016JC011970>.
- Peng, G., W. N. Meier, D. J. Scott, and M. H. Savoie, 2013: A long-term and reproducible passive microwave sea ice concentration data record for climate studies and monitoring. *Earth Syst. Sci. Data*, **5**, 311–318, <https://doi.org/10.5194/essd-5-311-2013>.
- Price, J. F., R. A. Weller, and R. Pinkel, 1986: Diurnal cycling: Observations and models of the upper ocean response to diurnal heating, cooling, and wind mixing. *J. Geophys. Res.*, **91**, 8411–8427, <https://doi.org/10.1029/JC091iC07p08411>.
- Pritchard, H. D., S. R. Ligtenberg, H. A. Fricker, D. G. Vaughan, M. R. Van Den Broeke, and L. Padman, 2012: Antarctic ice-sheet loss driven by basal melting of ice shelves. *Nature*, **484**, 502–505, <https://doi.org/10.1038/nature10968>.
- Reeve, K. A., O. Boebel, T. Kanzow, V. Strass, G. Rohardt, and E. Fahrbach, 2016: Objective mapping of Argo data in the Weddell Gyre: A gridded dataset of upper ocean water properties. *Earth Syst. Sci. Data*, **8**, 15–40, <https://doi.org/10.5194/essd-8-15-2016>.
- Robertson, R., L. Padman, and M. D. Levine, 1995: Fine structure, microstructure, and vertical mixing processes in the upper ocean in the western Weddell Sea. *J. Geophys. Res.*, **100**, 18 517–18 535, <https://doi.org/10.1029/95JC01742>.
- Roquet, F., and Coauthors, 2013: Estimates of the Southern Ocean general circulation improved by animal-borne instruments. *Geophys. Res. Lett.*, **40**, 6176–6180, <https://doi.org/10.1002/2013GL058304>.
- , and Coauthors, 2014: A Southern Indian Ocean database of hydrographic profiles obtained with instrumented elephant seals. *Sci. Data*, **1**, 140028, <https://doi.org/10.1038/sdata.2014.28>.
- , and Coauthors, 2017: MEOP-CTD in-situ data collection: A Southern ocean Marine-mammals calibrated sea water temperatures and salinities observations—2017-11 release. SEANOE, accessed 10 May 2018, <https://doi.org/10.17882/45461>.
- Semtner, A. J., 1976: A model for the thermodynamic growth of sea ice in numerical investigations of climate. *J. Phys. Oceanogr.*, **6**, 379–389, [https://doi.org/10.1175/1520-0485\(1976\)006<0379:AMFTTG>2.0.CO;2](https://doi.org/10.1175/1520-0485(1976)006<0379:AMFTTG>2.0.CO;2).
- Toole, J. M., M. L. Timmermans, D. K. Perovich, R. A. Krishfield, A. Proshutinsky, and J. A. Richter-Menge, 2010: Influences of the ocean surface mixed layer and thermohaline stratification on Arctic Sea ice in the central Canada basin. *J. Geophys. Res.*, **115**, C10018, <https://doi.org/10.1029/2009JC005660>.
- Wong, A. P. S., and S. C. Riser, 2011: Profiling float observations of the upper ocean under sea ice off the Wilkes Land coast of Antarctica. *J. Phys. Oceanogr.*, **41**, 1102–1115, <https://doi.org/10.1175/2011JPO4516.1>.
- Worby, A. P., C. A. Geiger, M. J. Paget, M. L. Van Woert, S. F. Ackley, and T. L. DeLiberty, 2008: Thickness distribution of Antarctic sea ice. *J. Geophys. Res.*, **113**, C05S92, <https://doi.org/10.1029/2007JC004254>.